International Journal of Nanomedicine Dovepress

Open Access Full Text Article ORIGINAL RESEARCH

Yam Carbon Dots Promote Bone Defect Repair by Modulating Histone Demethylase 4B

QianYang Chen[1,*], Shuo Liu[1,*], Yuhan Wang[1,*], MeiChen Tong[2], HaiBo Sun[2], Ming Dong[1], Yun Lu[1], WeiDong Niu[1], LiNa Wang[1]

[1]Department of Endodontics and Periodontics, College of Stomatology, Dalian Medical University, Dalian, Liaoning, 116044, People's Republic of China; [2]Academician Laboratory of Immune and Oral Development & Regeneration, Dalian Medical University, Dalian, Liaoning, 116044, People's Republic of China

*These authors contributed equally to this work

Correspondence: WeiDong Niu; LiNa Wang, Email 13840886663@139.com; wanglina@dmu.edu.cn

Introduction: Chronic apical periodontitis is a typical inflammatory disease of the oral cavity, the pathology is characterized by an inflammatory reaction with bone defects in the periapical area. Chinese medicine is our traditional medicine, Carbon Dots (CDs) are a new type of nanomaterials. The purpose of this study was to prepare Yam Carbon Dots (YAM-CDs) to investigate the mechanism of action of YAM-CDs on bone differentiation in vivo and in vitro.

Methods: We characterized YAM-CDs using transmission electron microscopy (TEM), Fourier Transform Infrared Spectrometer (FTIR), X-Ray Diffraction (XRD) and photoluminescence (PL). CCK-8 assay, Real-time qPCR, and Western Blot were conducted using bone marrow mesenchymal stem cells (BMSCs) to verify that YAM-CDs promote osteoblast differentiation. In addition, we investigated the role of YAM-CDs in promoting bone formation in an inflammatory setting in an in vivo mouse model of cranial defects.

Results: The results of TEM and PL showed that the YAM-CDs mostly consisted of the components C1s, O1s, and N1s. Additionally the average sizes of YAM-CDs were 2–6 nm. The quantum yield was 4.44%, with good fluorescence stability and biosafety. Real-time qPCR and Western blot analysis showed that YAM-CDs promoted osteoblast differentiation under an inflammatory environment by regulating expression of histone demethylase 4B (KDM4B). In vivo, results showed that YAM-CDs effectively repaired cranial bone defects in a mouse model and reduced the expression of inflammatory factors under the action of lipopolysaccharides (LPS).

Conclusion: YAM-CDs promoted the proliferation and differentiation of osteoblasts by regulating the expression of KDM4B to repair cranial bone defects in mice under an LPS-induced inflammatory milieu, which will provide a new idea for the treatment of clinical periapical inflammation and other bone defect diseases.

Keywords: traditional Chinese medicine, carbon dots, YAM, bone defect, KDM4B

Introduction

Chronic apical periodontitis is a typical inflammatory disease of the oral cavity,[1] which is mainly triggered by bacterial infection. The pathology is characterized by an inflammatory reaction with bone defects in the periapical area, which ultimately leads to tooth loss.[2] How to regenerate destroyed periapical alveolar bone and periodontal tissues is a critical scientific problem that needs to be solved urgently. Current research is focused on tissue engineering and regenerative medicine. Biomaterials with nanostructures have significant advantages in bone defect repair due to their ability to reassemble new bone on the nanoscale, which is closer to the natural bone structure.[3]

Nanostructure and the related structure-performance are the most popular topics in nanomedicine,[4] particularly, the core-shell nanostructures, representing an outer-inner spatial relationship, can support a wide variety of strategies for developing functional nanomaterials, which include core-shell nanoparticles,[5] core-shell nanofibers[6] and their combinations.[7] Carbon dots (CDs), a type of fluorescent nanomaterials derived from a carbon source, consist of carbon

Received: 9 May 2024
Accepted: 5 October 2024
Published: 16 October 2024

cores and surface groups and thus representing a new kind of structural nanomedicine. They are usually less than 10 nm in size,[8–11] and are often used in bioengineering-related fields due to their unique physical and optical properties.[12] CDs have broadband absorption and size-dependent photoemission at 260–320 nm, strong photoluminescence quantum yields, tunable surfaces with minimal toxicity, and appropriate electron transport properties.[13] Gogoi et al[14] created peptide composites of CDs implanted in tannic acid and polyurethane matrices for in vivo bone regeneration and showed that the nanocomposites of CDs exhibited good mechanical properties and osteogenic activity in osteoblast studies. Due to their unique structure and function, CDs have gained widespread attention in the biomedical field.

Based on the concept of green chemistry, the use of "green" substances as raw materials is becoming a hot topic in production research. Traditional Chinese medicine (TCM) is one of these green precursors and has received widespread attention for its unique medical benefits.[15] Due to the complexity of the composition of Chinese medicines, the efficacy of which cannot be fully expressed, researchers have attempted to prepare a variety of Chinese medicinal substances at the nanoscale. It has been discovered that TCMs can be used as raw materials to produce novel nanomaterials under high-temperature conditions, known as TCM carbon dots (TCMs-CDs),[16] which include TCM charcoal medicines, TCM extracts, and small molecules of TCM.[17] TCMs-CDs, which are CDs prepared from TCM as raw materials, have the advantages of low toxicity and high biocompatibility. In this study, we synthesized YAM-CDs using the traditional Chinese medicine YAM as a precursor, which contains active ingredients of TCM and chemicals derived from YAM, and also retains the medicinal value and bioactivity of TCM, compared with the general carbon dots. Further study of their biological functions will contribute to their wide application in the fields of bone defect repair, drug delivery and targeted therapy.

The Chinese Yam (YAM), *Dioscorea opposita*, through the mountain dragon, etc.,[18] was first recorded in the Shennong Ben Cao Jing (Classic of the Materia Medica of the Divine Husbandman), in which it is recorded that it is used to treat "the main injuries in the middle of the body, supplementing weakness and wonkiness, removing cold and heat evil qi, tonifying the middle of the body and benefiting the strength of qi, growing muscles, taking it for a long time to be smart in the ears and eyes", as well as having other therapeutic effects.[19] Chemical composition studies have found that YAM contains mainly polysaccharides, starch, proteins, etc., and its rhizomes contain diosgenin and bibenzyl analogs.[20] Biological effects mainly include anti-tumor and anti-inflammatory properties, promoting the proliferation and differentiation of osteoblasts and inhibiting the formation of osteoclasts.[21] It also has characteristics of low toxicity, few adverse reactions, economy, and safety. It is widely used in the clinic to treat diabetes, cancer, osteoarthritis, and other diseases. Exosome-like nanovesicles derived from YAM have been demonstrated to promote the growth, differentiation, and mineralization of MC3T3-E1 cells by triggering the BMP-2/p-p38 pathway. This, in turn, results in an upregulation of the expression of bone differentiation markers, such as osteopontin, alkaline phosphatase, and type I collagen.[22] According to research by Jin et al, YAM extract stimulates collagen production, matrix mineralization, and alkaline phosphatase activity, all of which support the osteogenic function of osteoblasts and the maturation of the bone matrix.[23] However, TCM extracts themselves are slow to take effect and have a long duration of treatment, whereas TCM-CDs increase their bioavailability.

Histone methylation is one of the essential types of epigenetic regulation that modulates the activation of multiple signaling pathways in physiological and pathological processes.[24] Histone demethylase 4B (KDM4B) mainly functions in transcriptional expression of genes such as demethylation H3K9me3/me2, DNA damage repair, etc., and is widely expressed in both osteoblasts and osteoclasts.[25] Abnormally high levels of KDM4B in rheumatoid arthritis have been found to promote growth, migration, and invasion of fibroblast-like synoviocytes and inhibit apoptosis through the signal transducer and activator of transcription 3 (STAT3) signaling pathway.[26] KDM4B is also involved in cartilage and fat formation by mesenchymal stem cells (MSCs). It was found that transforming growth factor beta (TGF-β) significantly induced the expression of KDM4B in MSCs, which was stimulated by TGF-β to remove the inhibitory H3K9me3 methylation mark from the SOX9 promoter, thereby inducing the expression of a significant regulator of cartilage formation.[27] By establishing KDM4B knockout mice, Deng et al found that deletion of the epigenetic factor KDM4B in MSCs may exacerbate skeletal aging and osteoporosis by decreasing bone formation and increasing bone marrow fat through increased H3K9me3; importantly, deletion of KDM4B promotes bone loss induced by a high-fat diet, further supporting the idea that KDM4B is a *bona fide* epigenetic factor associated with bone formation.[28]

YAM-CDs have the potential to serve as a novel nanoscale drug derived from TCM that promotes both bone formation and effective anti-inflammatory properties. To test this hypothesis, we first prepared YAM-CDs by hydrothermal synthesis, verified whether YAM-CDs were successfully developed by structural characterization and optical characterization, and examined the role of YAM-CDs in promoting osteogenic differentiation of bone marrow mesenchymal stem cells (BMSCs). The inflammatory microenvironment of osteoblast precursor cells was also constructed to test the effect of the YAM-CDs on osteoblasts. The repair effect of YAM-CDs on inflammatory bone defects in vivo was elucidated by establishing a mouse cranial bone defect model. This study showed that YAM-CDs is expected to be a candidate for the clinical repair of inflammatory bone defects.

Material and Methods

Synthesis of YAM-CDs

YAM-CDs were synthesized by the hydrothermal method using YAM (Tong Ren Tang, Beijing, China) as a precursor (Figure 1). After dissolving 1 g of YAM powder in 20 mL of distilled water, the mixture was put in a high pressure reactor (Chang Yi Equipment Co., Xian, China), centrifuged for 15 min at 180°C and 16060 *g*, and allowed to settle for 7 days before being dialyzed and kept at 4°C.

Next, 30 g of the above herbal YAM powder was mixed with 10 times the amount of distilled water and soaked for 2 h, then decocted by boiling on a high heat for 30 min, twice. After cooling to room temperature, 95% ethanol was added (so that the concentration of ethanol in the liquid was 60%), then the precipitate was centrifuged, and the supernatant was removed; the decoction was concentrated to 1 g/mL as the stock solution, bacteria were filtered out through a microporous filter membrane, and the decoction was put into sterile bottles for later use.

The extracts were obtained based on the approaches of the International Standard Organization (ISO 10993–5). Prior to cell testing, the already prepared YAM-CDs in sterile vials were filter-sterilized with a 0.22 μm filter (Millipore, USA) to maintain sterility before subsequent cell experiments.

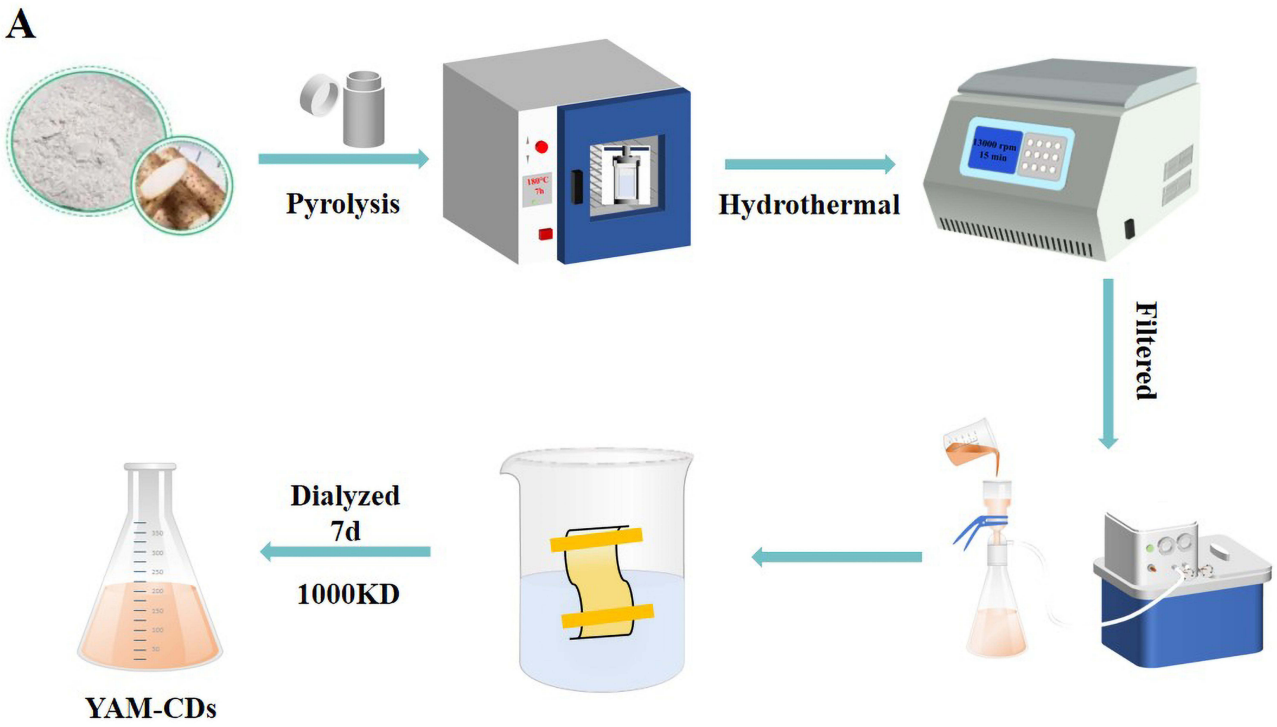

Figure 1 Flowchart of YAM-CDs production.

Characterization and Identification of YAM-CDs

The YAM-CDs solution was dripped onto a nanoscale carbon grid for TEM and allowed to stand at room temperature for 30 min. At the end of this time, any residual liquid on the carbon grid was blotted using filter paper, and the lattice spacing of the YAM-CDs was detected using a transmission electron microscope (Tecnai G220, FEI Company, Hillsboro, OR, USA). X-ray diffraction (XRD) (D8 ADVANCE A25X, Karlsruhe, Germany) was used to analyze the composition of the material and the structure of the internal molecules with a wide-angle detection of 5°–90° and a detection speed of 10°/min. A Fourier transform infrared spectrometer (FTIR) (Nicolet™ Is10; Thermo Fisher Scientific, Waltham, MA, USA) was set with a scanning range of the spectrum from 4000 to 5000 cm^{-1} to detect the chemical structure and surface functional groups of YAM-CDs, while Zeta potential (Nano S Malvern, Guang Zhou, China) was used to investigate the self-stability of YAM-CDs. The YAM-CDs solution was lyophilized, and samples of the lyophilized dried powder were prepared for X-ray photo-electron spectroscopy (XPS) (D8 ADVANCE A25X, Germany), successfully pressed, and then tested on the machine.

The UV spectra of the YAM-CDs dialysate were analyzed by UV-visible spectroscopy (UV-vis) (UV-2600, Shimadzu Corp., Kyoto, Japan) by taking an appropriate amount of YAM-CDs dialysate, preparing multiple dilutions and aspirating in 2 mL, then scanned with a scanning speed of 5 nm/s and a test wavelength range of 200–600 nm. The fluorescence characteristics of YAM-CDs were analyzed using photoluminescence (PL) (G9800A, Agilent Technologies, Santa Clara, CA, USA) with a scanning speed of 1200 nm/min, a test wavelength range of 200–600 nm, and a slit width of 10 nm. Using quinine sulfate as a reference, the quantum yield was calculated from the following equation: $Q = \frac{I_1}{I_2} \times \frac{A_2}{A_1} \times Q_2 \times \left(\frac{\eta_1}{\eta_2}\right)^2$ where I is the integral area under the emission spectrum, I_1 represents the integral area under the emission spectrum of YAM-CDs to be tested, and I_2 represents the integral area under the emission spectrum of quinine sulfate; A represents the UV-vis absorbance under the fluorescence excitation wavelength, A_1 represents the integral area under the emission spectrum of YAM-CDs to be tested, and A_2 represents the integrated area under the emission spectrum of quinine sulfate; Q_2 represents the quantum yield of quinine sulfate (Known, $Q_2 = 0.54$); η is the refractive index, η_1 represents the refractive index of YAM-CDs to be tested, and η_2 represents the refractive index of quinine sulfate.

Cell Culture

Male C57BL/6J mice aged 6–8 weeks were selected and provided by the Specific Pathogen-Free (SPF) Experimental Animal Center of Dalian Medical University (China). The experiment was validated and approved by the Ethics Committee of Dalian Medical University (approval number: AEE21061). Bone marrow was aseptically isolated from femurs and tibiae of mice by rinsing them with α-Modified Minimum Essential Medium (α-MEM) (Hyclone, Logan, UT, USA) containing 20% Fetal Bovine Serum (FBS) (ScienCell Research Laboratories, Carlsbad, CA, USA), 100 U/mL penicillin and 100 μg/mL streptomycin (ScienCell, USA). Erythrocytes were lysed (Coolaber, Beijing, China) and the cells were cultured at 37°C with 5% CO_2. Cell passaging was performed and the cells were passed to the third generation for spare when the fusion rate of wall-adherent cells was greater than 80%.

MC3T3-E1 cells (Procell, Wuhan, China) were cultured in α-MEM containing 10% FBS, 1% penicillin and 100 μg/mL streptomycin, in a 37°C, 5% CO_2 incubator. When the cells reached 70–80% confluence, they were observed under an inverted microscope, and the cells were passaged for subsequent experiments.

Immunofluorescence Staining

BMSCs were inoculated into 6-well plates at 3×10^4 cells/well and fixed with 4% paraformaldehyde for 30 min, then the membrane was permeabilized using phosphate-buffered saline with Tween (PBST) for 20 min at room temperature. Next, cells were blocked with 10% goat serum (ZSGB-BIO, Beijing, China) at constant room temperature for 1 h, then antibodies to CD44 (1:200 dilution, ABclonal, Wuhan, China) and CD90 (1:200 dilution, ABclonal, Wuhan, China) were added separately and incubated at 4°C overnight. Next day, DyLight 549 (1:200 dilution, Abbkine, Redlands, CA, USA) fluorescently- labeled anti-rabbit secondary antibody was mixed and incubated for 1 h at room temperature, followed by

counterstaining with DAPI staining solution (Bioss, Beijing, China) for 10 min, and photographs were taken under an inverted microscope.

Flow Cytometry

Cells of the third generation of BMSCs were harvested and subjected to digestion with 0.25% trypsin for 5 min. Following this, 10% α-MEM was added to stop the digestion, and the cell pellets were rinsed with phosphate-buffered saline (PBS). The cells were then resuspended in PBS for cell counting, and the cell density was adjusted to 1×10^6 L^{-1}. Next, the cells were incubated for 30 min at 4°C with anti-mouse CD34-FITC, CD90-PE, or CD29-FITC antibodies (all from Elabscience, Wuhan, China), shielded from light, and then excess antibody was removed by washing with PBS. The cells were then subjected to flow cytometric analysis.

CCK-8 Assay

BMSCs at 2000 cells/well were inoculated into 96-well plates, and allowed to attach for 24 h. After gradient dilution, the prepared YAM solution and YAM-CDs solution were added to the corresponding wells and the plates were incubated for 0, 24, 48, and 72 h. At the end of the culture period, the medium was discarded and 100 μL CCK-8 solution (Biyuntian, Jiangsu, China), diluted in culture medium at a ratio of 1:9, was added to each well, and the cells were returned to the incubator for 1 h. The results were determined by spectrophotometry at 450 nm.

Real-Time qPCR

BMSCs at 4×10^5 cells/well were inoculated into wells of 6-well plates and divided into a control group, YAM group, and YAM-CDs group. The groups were treated with simple culture medium, YAM (1×10^{-4} g/mL), or YAM-CDs (1 g/mL), respectively. Cell samples were collected after 3 days of continuous culture, and gene expression levels of histone demethylase 4B (KDM4B), alkaline phosphatase (ALP), osteopontin (OPN), runt-related transcription factor 2 (Runx2) were analyzed by real-time qPCR.

Total RNA was extracted from the cells according to the instructions provided in the Cellular Total RNA Extraction Kit (Sangon Biotech, Shanghai, China), and a Nano Drop® ND-1000 instrument (Thermo Fisher Scientific) was used to determine the concentration and purity. RNA was reverse transcribed into cDNA according to the instructions provided with the Evo M-MLV Reverse Transcription Kit (Accurate Biology, Hunan, China), and the reaction solution was prepared according to the instructions of the SYBR® Green Pro Taq HS qPCR kit for real-time qPCR experiments. The primers for the mouse-related genes to be detected were designed and synthesized by Gemma Genetics Ltd. (address), as shown in Table 1. The reaction conditions were 95°C 30s; 95°C 5s; 60°C 30s for 40 cycles; followed by 95°C 15s; 60°C 30s; 95°C 15s. GAPDH was utilized as the housekeeping gene. The relative mRNA concentrations were measured by $E = 2^{-\Delta\Delta Ct}$, and the key threshold cycle (CT) value was examined in each reaction.

Table 1 Primer Sequences of Mouse Genes

Primer	Sequences
ALP	Forward: 5′-TGAATCGGAACAACCTGACTGA-3′
	Reverse: 5′-GAGCCTGCTTGGCCTTACC-3′
Runx2	Forward: 5′-CCTCTGGCCTTCCTCTCTCA-3′
	Reverse: 5′-TAGGTAAAGGTGGCTGGGTAGTG-3′
OPN	Forward: 5′-TGCAGTGGTTCGGAGCAAC-3′
	Reverse: 5′-TTTTCTGTGCGCCAGCTATAC-3′
KDM4B	Forward: 5′-GCAACCCAGTGGACGTCAGT-3′
	Reverse: 5′-CATGCGCACAGGTCACATG-3′
GAPDH	Forward: 5′-GGCACAGTCAAGGCTGAGAATG-3′
	Reverse: 5′-ATGGTGGTGAAGACGCCAGTA-3′

Western Blotting

BMSCs were treated and cultured as described above. Western blotting was performed to detect the levels of OPN and Runx2 protein expression.

Protein lysates were prepared at the ratio of RIPA (Solarbio, Beijing, China): PMSF (Solarbio, China) = 100:1, and total cellular proteins were extracted according to the instructions; a standard curve was drawn and the protein concentration of the samples was calculated using a BCA kit (Elabscience, Wuhan, China). The samples were separated by electrophoresis on a polyacrylamide gel (Yamei, Shanghai, China), followed by electroblotting onto a nitrocellulose (NC) membrane at 200 mA for 1.5 h. The membrane was then blocked with 5% skimmed milk powder (BD Biosciences, Franklin Lakes, NJ, USA) for 2 h at room temperature. The primary antibodies (OPN (1:1000 dilution; Abcam, Cambridge, MA, USA), Runx2 (1:1000 dilution, Huaan, Shandong, China), and GAPDH (1:5000 dilution; ABclonal) were diluted in TBST, and the NC membrane was incubated in the primary antibody at 4°C overnight. Next day washed membrane, the HRP-conjugated goat anti-rabbit IgG was prepared (1:5000 dilution, ABclonal, China) and the NC membrane was incubated in the secondary antibody for 1 h at room temperature. After this washed membrane, the ECL luminescent solution (Yamei, Shanghai, China) was diluted 1:1, then the membrane was exposed, and developed using a gel imaging system, and the imaged bands were analyzed semi-quantitatively using Image J software (NIH, Bethesda, MD, USA).

Alkaline Phosphatase (ALP) Staining

After being passaged and resuspended, the BMSCs were distributed evenly at a density of 2×10^6 cells/well in 6-well plates, and divided into three groups: control, YAM and YAM-CDs. When the cells increased to 50% confluence, 2 mL of osteogenic induction solution was added to each well. Then, simple culture medium, YAM (1×10^4 g/mL), and YAM-CDs (1 g/mL) were added to the appropriate wells to continue the culture. The color of the culture medium was observed, 3-day replacement if necessary, and after 7 days of induction the cells were subjected to alkaline phosphatase activity assay. To perform the assay, the cultured cells were washed in PBS, fixed in 1 mL of 4% paraformaldehyde in PBS for 30 min, followed by washing in double-distilled water (DDW). The reaction solution was prepared according to the manufacturer's instructions (Biyuntian, China), then added at 1 mL/well, incubated for 15 min at 37°C protected from light, then washed in DDW and observed under a light microscope.

Cell Migration Assay to Evaluate the Migratory Ability of BMSCs

After being passaged and resuspended, BMSCs were inoculated at a density of 1×10^5 cells/well into wells of 6-well plates, and 1.5 mL of α-MEM complete medium was added to each well. The cells were then divided into three groups: control, YAM and YAM-CDs, and a 100 μL pipette tip was used to make two parallel transverse scratches across the center of each well. The wells were then rinsed with PBS and fresh medium was added. Photographs were taken under the microscope after 0, 6, and 12 h. Photographs of more than 5 different fields of view were captured to record and analyze the degree of cell migration, and the experiment was repeated three times.

Creation of a Cellular Inflammatory Microenvironment and Detection of the Expression of mRNA, Protein of KDM4B and Osteogenesis-Related Factors in MC3T3-E1 Cells Under the Influence of YAM-CDs

Digested MC3T3-E1 cells were inoculated into 6-well plates at 4×10^5 cells/well, and divided into six groups: control group (culture medium alone), lipopolysaccharide (LPS) group (1 mg/mL), YAM group (1×10^{-4} g/mL), YAM-CDs group (1 g/mL), 1 mg/mL LPS+YAM group (1×10^{-4} g/mL) and 1 mg/mL LPS+YAM-CDs group (1 g/mL). Cell samples were collected after 3 days of continuous treatment, and expression levels of KDM4B and the osteogenesis-related factors ALP and Runx2 genes and proteins were analyzed by real-time qPCR and Western blotting. The expression of ALP was analyzed by ALP staining after 7 days of culture in the above groups.

Knockdown of KDM4B and Detection of mRNA and Protein Expression of Osteogenesis-Related Factors

MC3T3-E1 cells were inoculated into 6-well plates at a density of 1×10^6 cells/well. After the cells were well-adhered, 1 mg/mL LPS was added to establish an inflammatory environment, and transfection was carried out 24 h later when the cell density reached 70–80%. Cells were divided into an NC group, an LPS+KDM4B-siRNA group, an LPS+KDM4B-siRNA+YAM group, and an LPS+KDM4B- siRNA+YAM-CDs group. KDM4B-siRNA was synthesized by GenePharma (Shanghai, China), and the synthetic sequence was 5′-ACUAAUUUUGUCUGCGCAGGTT-3′. Cell transfection was performed according to the instructions provided with the Liposome 3000 transfection agent (Thermo Fisher Scientific, China). After 6 h the medium was discarded and the drug solution was added. After 24 h of treatment, cells were collected, genes and proteins were extracted, and the transfection rate and expression of ALP and Runx2 genes and proteins were analyzed by real-time qPCR and Western blotting.

Repair of Cranial Defects in a Mouse Model by YAM-CDs

The experimental animals were C57BL/6J mice, SPF grade, male, 8-weeks-old, weighing 20–25 g, provided by the SPF Animal Experiment Center of Dalian Medical University. All animal experiments were validated and approved by the Ethics Committee of Dalian Medical University (approval number: AEE21061) and performed in accordance with the guidelines set forth in the Guide for the Care and Use of Laboratory Animals published by the National Institutes of Health.

An incision approximately 1 cm long was made along the median line of the cranial vault of each mouse, and the bones were removed at the cranial vault using a dental slow-speed grinder with a speed of 1500 rpm and a 1.5-mm-diameter split drill. Two weeks after operation, the mice were euthanized first, the cranial bones of the five groups (control group, GEL group, GEL+YAM-CDs group, GEL+LPS group, GEL+LPS+YAM-CDs group) of mice were harvested, fixed in 4% paraformaldehyde, decalcified in 10% ethylene diamine tetraacetic acid (EDTA); dehydrated in an ethanol gradient, and embedded in wax, then cleared with xylene (SolarBio, Beijing, China). Blocks were cut into consecutive sections of 5 μm thickness, floated in a water bath, lifted onto slides and baked in an 37°C oven for 3–4 h.

Hematoxylin-eosin (HE) staining (Biyuntian, China): sections were subjected to routine dewaxing and rehydration, stained in hematoxylin for 5 min, rinsed in 1% hydrochloric acid alcohol differentiation for 5s followed by warm water anti-blue for 10 min, then stained with eosin for 1 min. Sections were then dehydrated with ethanol, cleared with xylene, and mounted with a small drop of neutral gum to cover the tissue completely.

Masson's trichrome staining (Suolaibao, Beijing, China): sections were routinely dewaxed and rehydrated, stained with Weigert's iron hematoxylin for 10 min, differentiated with acidic ethanol differentiation solution for 15s, returned to the blue with Masson's bluing solution for 1 min, stained with Lichun red magenta staining solution for 5 min, washed with a weak acidic working solution for 1 min, washed with phosphomolybdenum solution for 2 min, stained with aniline blue staining solution for 2 min, then dehydrated with ethanol, cleared with xylene, and sealed with neutral gum for 2 min. Photomicrographs were captured under a light microscope.

Immunohistochemical (IHC) staining: samples were processed by routine dewaxing to water, followed by antigen repair with citric acid and microwave treatment on high (5 min) or medium (10 min) power. Next, endogenous peroxidase was blocked for 10 min, followed by serum containment for 15 min. Primary antibodies (KDM4B (1:200 dilution; ABclonal, China), osteocalcin (OCN) (1:200 dilution; Abcam, USA), and tumor necrosis factor alpha (TNF-alpha) (1:200 dilution; Huaan, China)) were incubated on the slides for 12 h (overnight at 4°C) and next day the secondary antibody, goat anti-mouse IgG polymer antibody (IgG) (1:250 dilution; Abcam, USA) was incubated for 15 min. Finally DAB solution (Biyuntian, China) was added and incubated, protected from light for 5 min, then slides were rinsed under running water for 5 min. Nuclear counter-staining was performed using hematoxylin for 10 min, followed by hydrochloric acid alcohol differentiation for 30s then anti-bluing in warm water for 10 min, and the color was observed under a light microscope. The slices were then dehydrated with ethanol, cleared with xylene, and sealed with neutral gum. Three discontinuous sections were selected for each group, and the same measurement area was chosen

for each section. The IHC staining results of KDM4B, OCN, and TNF-α were analyzed semi-quantitatively using Image Pro Plus software (Media Cybernetics, Rockville, MD, USA).

Statistical Analysis

All the above data are expressed as the mean ± standard deviation (SD). SPSS 17.0 software (SPSS Inc., Chicago, IL, USA) was used for statistical analysis. Tukey's test ($\alpha = 0.05$) was used for comparison between two groups, and one-way analysis of variance (ANOVA) was used for comparison between multiple groups. The difference was considered statistically significant when the p-value was < 0.05.

Results

Characterization and Identification of YAM-CDs

YAM-CDs were prepared by hydrothermal synthesis, which is in line with the process of decoction of TCM, and no toxic solvents were added in the preparation process, which ensured the biosafety of YAM-CDs to the greatest extent possible.

As shown in (Figure 2A and B), the morphology and particle size distribution of YAM-CDs were examined by TEM and HRTEM (high-resolution TEM). TEM showed that the YAM-CDs were spherical, with a particle size of 2–6 nm. HRTEM showed that the YAM-CDs had a graphite-like crystal backbone with a lattice spacing of 0.22 nm, consistent with the surface of graphitic carbon. The zeta potential is shown in (Figure 2C), with YAM-CDs having a zeta potential of −14 mV, which indicated that YAM-CDs is more stable in solution. From the FTIR spectra of YAM-CDs, shown in (Figure 2D), we found five significant absorption peaks at 3350.40 cm^{-1}, 2925.78 cm^{-1}, 1667.64 cm^{-1}, 1370.03 cm^{-1}, and 1152.65 cm^{-1}. Among them, the broad peak at 3350.40 cm^{-1} was related to the O-H/N-H bond; the absorption peak at 2925.78 cm^{-1} was mainly attributed to the stretching vibration of the C-H bond; the peak at 1667.64 cm^{-1} corresponded to the stretching vibration of C=C in the benzene ring; and the absorption peak at 1370.03 cm^{-1} was observed to represent the characteristic absorption peak of the C-N bond, while the absorption peak at 1152.65 cm^{-1} represented the presence of C-O-C bonds in YAM-CDs. The diffraction pattern of the YAM-CDs is shown in (Figure 2E), with a significant diffraction peak at a 2-Theta angle of 21.66°, which was due to the amorphous carbon being composed in a somewhat random manner. The optical properties of YAM-CDs are shown in Figure 2F and G. The UV-Vis spectra of the aqueous solution of YAM-CDs exhibited a broad absorption pattern descending from 200 nm, but there was no prominent peak (Figure 2F). The results of the PL spectra of YAM-CDs (Figure 2G) showed that YAM-CDs had an excitation-dependent feature, at the excitation wavelength (EX) of 405 nm, emission wavelength (EM) of 510 nm, and YAM-CDs appeared colored. The quantum yield of YAM-CDs was calculated to be 4.44%.

The composition of YAM-CDs is shown in the XPS spectra (Figure 3A–D). The YAM-CDs were mainly composed of the elements C1s, O1s, and N1s, with relative percentages of 80.34%, 14.34%, and 5.32%, respectively. The elements C, O, and N may correspond to C—C, C—OH, CüO, C—N, and C—O—C; heavy metal elements (Fe and Al) were not detected, proving non-toxicity. With the above experimental results we successfully prepared and characterized YAM-CCDs.

Successful Cell Isolation of BMSCs

Immunofluorescence experiments (Figure 4A) showed high expression of the surface markers CD44 and CD90 by BMSCs. Flow cytometric analysis (Figure 4B–D) showed that expression levels of the surface markers CD29 and CD90 by BMSCs were 99.4% and 99.5%, respectively, which were strongly positive, and the expression of CD34 was 8.5%, which was considered negative. Thus, we successfully isolated, cultured, and characterized BMSCs.

Screening of Optimal Concentration of YAM-CDs Acting on BMSCs

CCK-8 results (Figure 5A) showed that after BMSCs were treated with YAM for 48 or 72 h, cell proliferation was significantly inhibited at a concentration of 1×10^{-1} g/mL ($p < 0.05$), and the best cell proliferation-promoting activity was observed at 72 h with 1×10^{-4} g/mL of YAM ($p < 0.05$). The other time-points and concentrations tested did not significantly affect cell proliferation ($p > 0.05$). (Figure 5B) shows results after 24, 48, and 72 h of treatment with YAM-

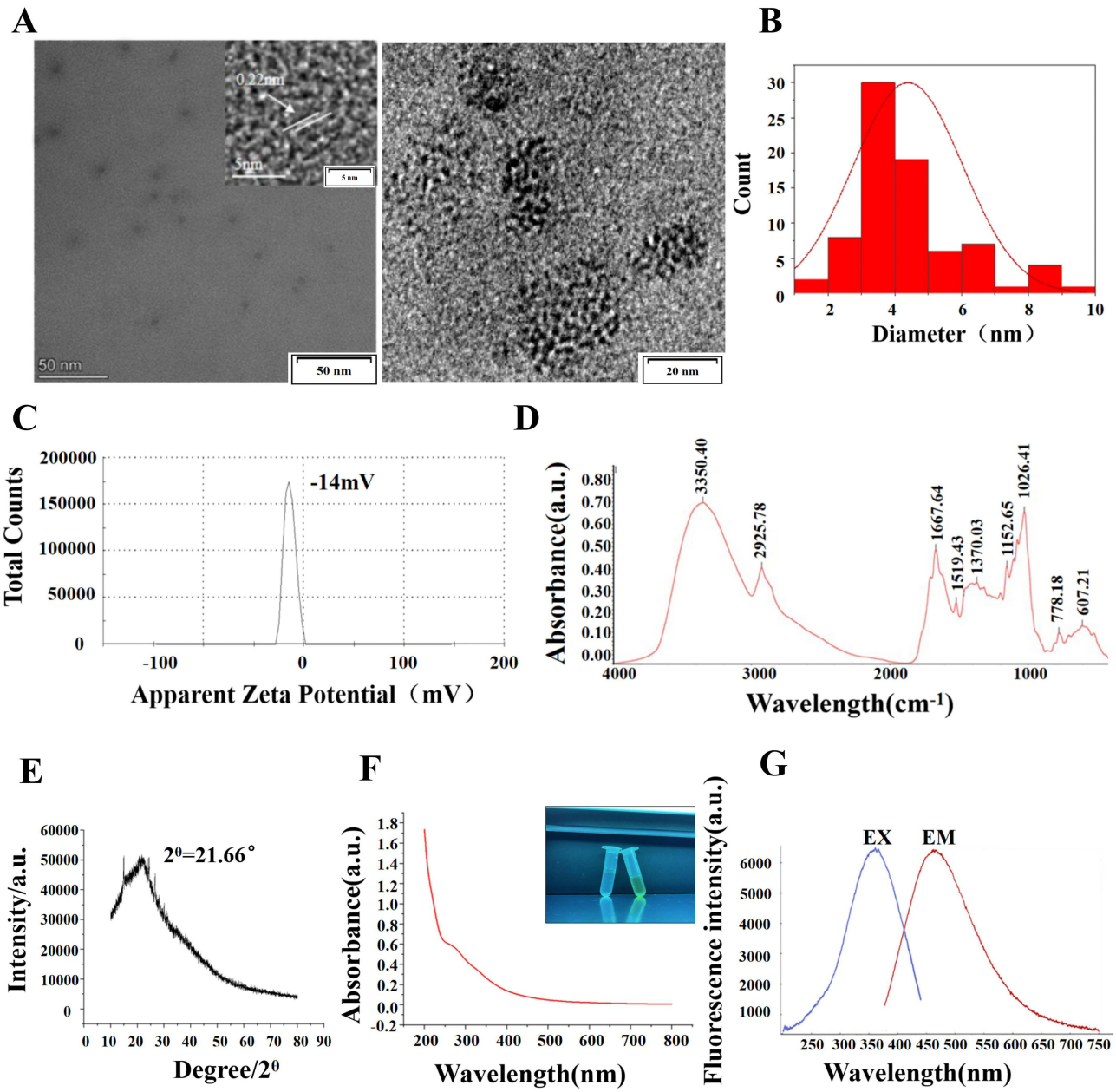

Figure 2 Characterization of YAM-CDs (**A**) Left: TEM image, right: HRTEM image. (**B**) Size distribution of YAM-CDs determined by TEM. (**C**) Zeta potential. (**D**) FTIR spectra. (**E**) XRD pattern. (**F**) UV-Vis spectra. (**G**) Photoluminescence spectra.

CDs; at 24 and 48 h, there was no effect on cell proliferation at any of the concentrations tested, while at 72 h YAM-CDs at 1 g/mL significantly promoted cell proliferation. All other concentrations showed no significant difference from the control group ($p > 0.05$). Based on these results, the concentration of YAM selected for subsequent experiments was 1×10^{-4} g/mL, and the concentration of YAM-CDs was 1 g/mL.

YAM-CDs Promote Proliferation and Differentiation of BMSCs

Cultured cells were divided into control, YAM, and YAM-CDs groups, and the results, shown in (Figure 5C–G), revealed that after 3 days of continuous treatment of BMSCs with YAM or YAM-CDs, expression of the bone formation signature markers OPN and Runx2 mRNA in the YAM-CDs group was significantly higher than that in the YAM group ($p < 0.05$), and the expression of proteins was in line with the trend of mRNA expression ($p < 0.05$). ALP staining of functionally-

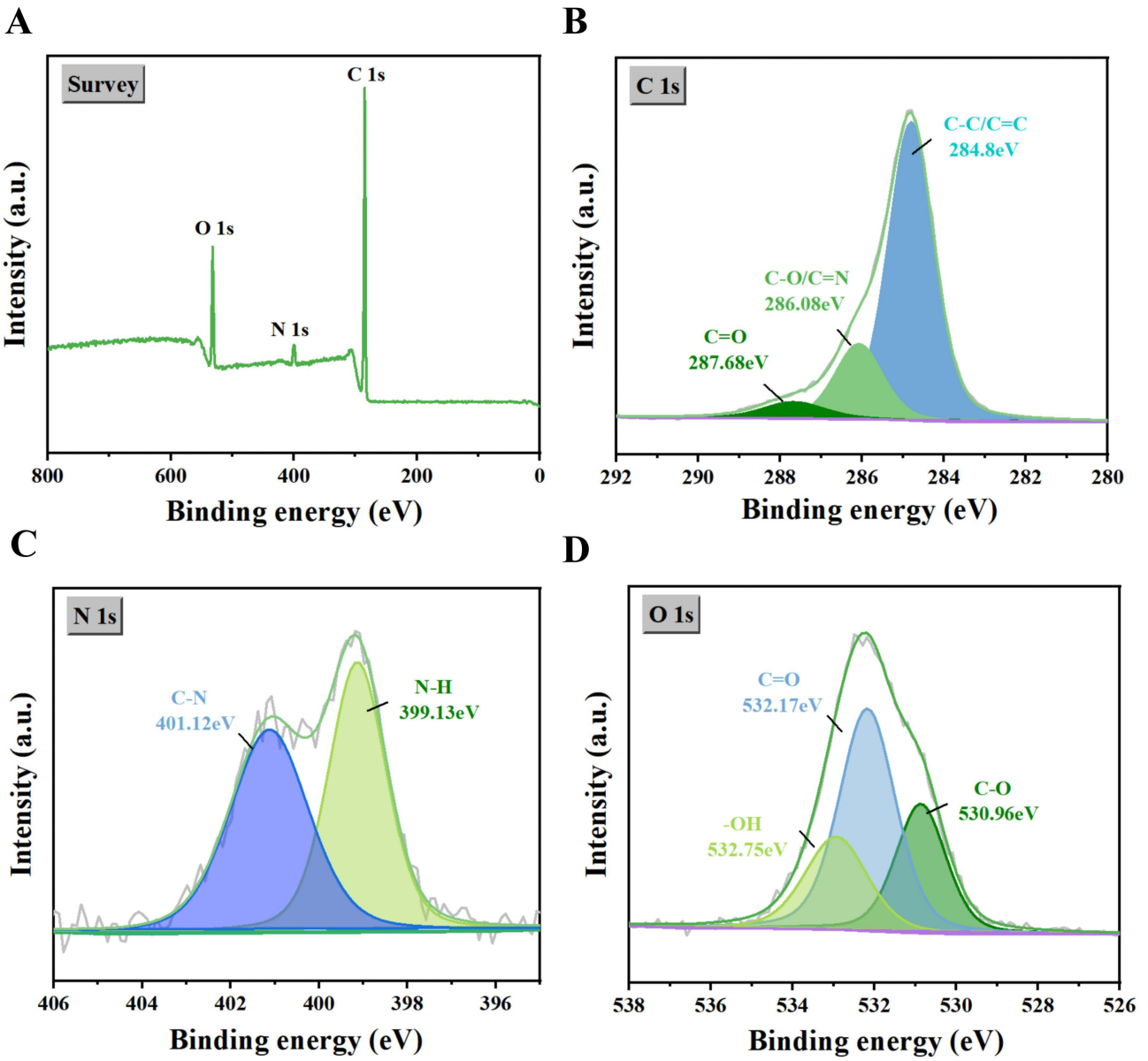

Figure 3 Surface composition and elemental analysis of YAM-CDs detected by XPS (**A**) XPS statistics of YAM-CDs. (**B**) XPS results of C1s. (**C**) XPS results of N1s. (**D**) XPS results of O1s.

active osteoblasts showed a positive reaction. Thus, both YAM and YAM-CDs significantly promoted the differentiation of BMSCs to osteoblasts, with the effect of YAM-CDs being superior to that of YAM, as shown in (Figure 5H and I) ($p < 0.05$). The results of scratch experiments (Figure 5J and K) showed that the YAM-CDs group significantly promoted the migration of BMSCs compared to the control and YAM groups ($p < 0.05$). The above results successfully demonstrated that YAM-CDs promotes osteogenic differentiation.

Effect of YAM-CDs Acting in a Microenvironment of LPS-Mediated Inflammation on the Expression of KDM4B and Osteogenesis-Related Factors in MC3T3-E1 Cells

As shown in (Figure 6A–G), in MC3T3-E1 cells, expression of the characteristic bone formation markers ALP and Runx2 in the YAM-CDs group was significantly higher than that in either the YAM group or the control group ($p < 0.05$), in which the expression of proteins was in line with the trend of mRNA expression. The expression trend of KDM4B mRNA and protein in the YAM-CDs group was in line with that of the osteogenesis-related factors, being

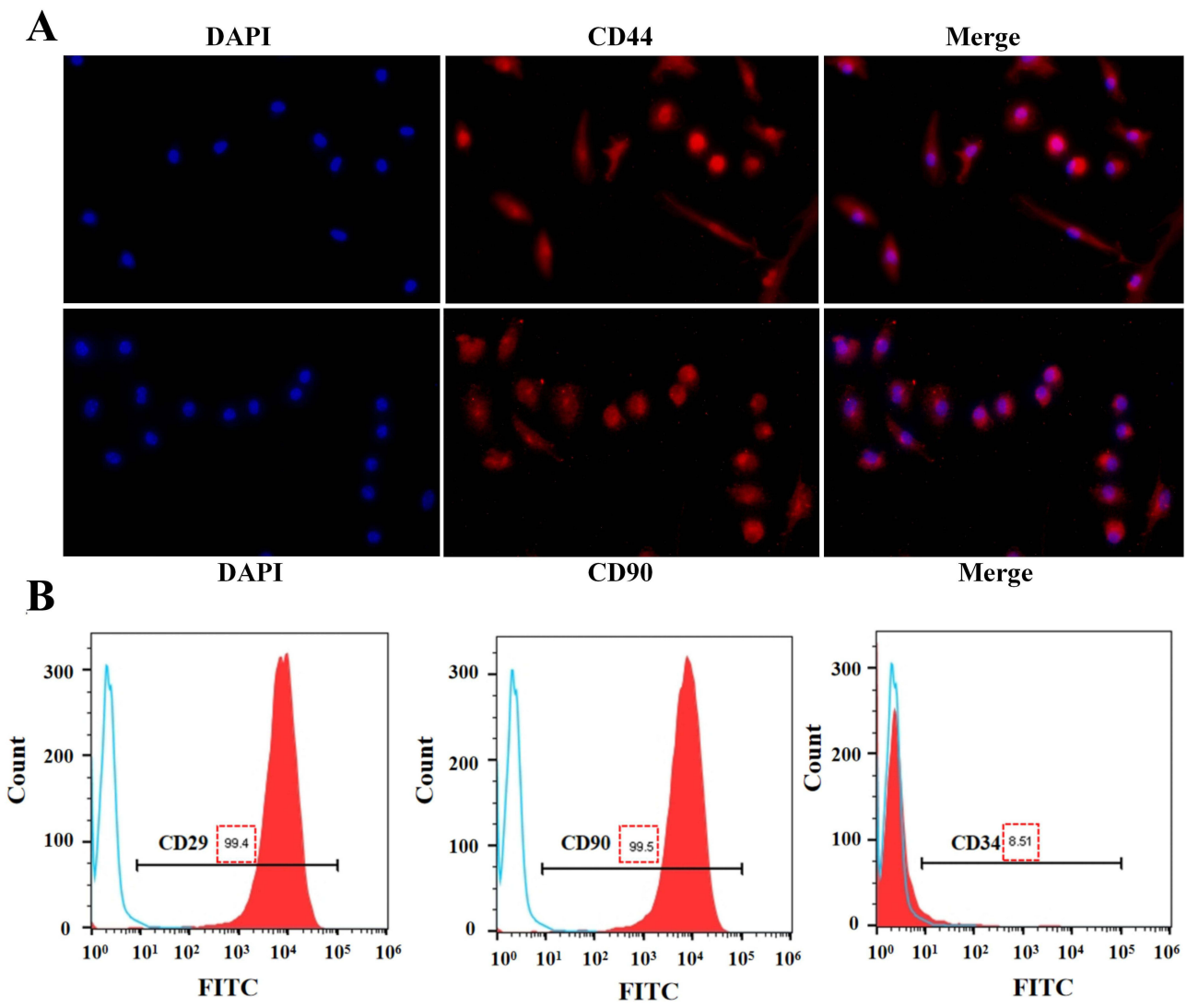

Figure 4 Isolation and identification of BMSCs (**A**) Immunofluorescence staining of BMSC surface markers CD44 and CD90. (Scale bar = 50 μm). (**B**) Flow cytometric analysis of the BMSC surface markers CD29, CD90 and CD34.

significantly higher than the YAM group or the control group ($p < 0.05$). Furthermore, expression of the bone formation signature factors ALP and Runx2 was significantly higher in the LPS+YAM-CDs group than in the LPS +YAM group or the LPS group ($p < 0.05$), and the expression of proteins was consistent with the trend of mRNA expression. Meanwhile, expression of KDM4B mRNA and protein in the LPS and LPS+YAM groups was significantly lower than that in the LPS+YAM-CDs group, and the expression trend was also consistent with that of the osteogenesis-related factors, suggesting that KDM4B was also one of the critical factors in promoting osteoblast differentiation.

MC3T3-E1 is a mouse embryonic osteoblast precursor cell line with high ALP activity and calcium nodule-generating capacity. As shown in (Figure 6H and I), after the addition of YAM or YAM-CDs to the cells, ALP staining of MC3T3-E1 cells was significantly increased compared with the control group ($p < 0.05$), and activity in the YAM-CDs group was higher than the YAM group ($p < 0.05$). In the LPS-mediated inflammatory microenvironment, ALP staining of MC3T3-E1 cells was significantly reduced. However, staining in the LPS+YAM-CDs and LPS+YAM groups remained higher than that of the LPS group ($p < 0.05$), and that in the LPS+YAM-CDs group was higher than that of the LPS +YAM group ($p < 0.05$).

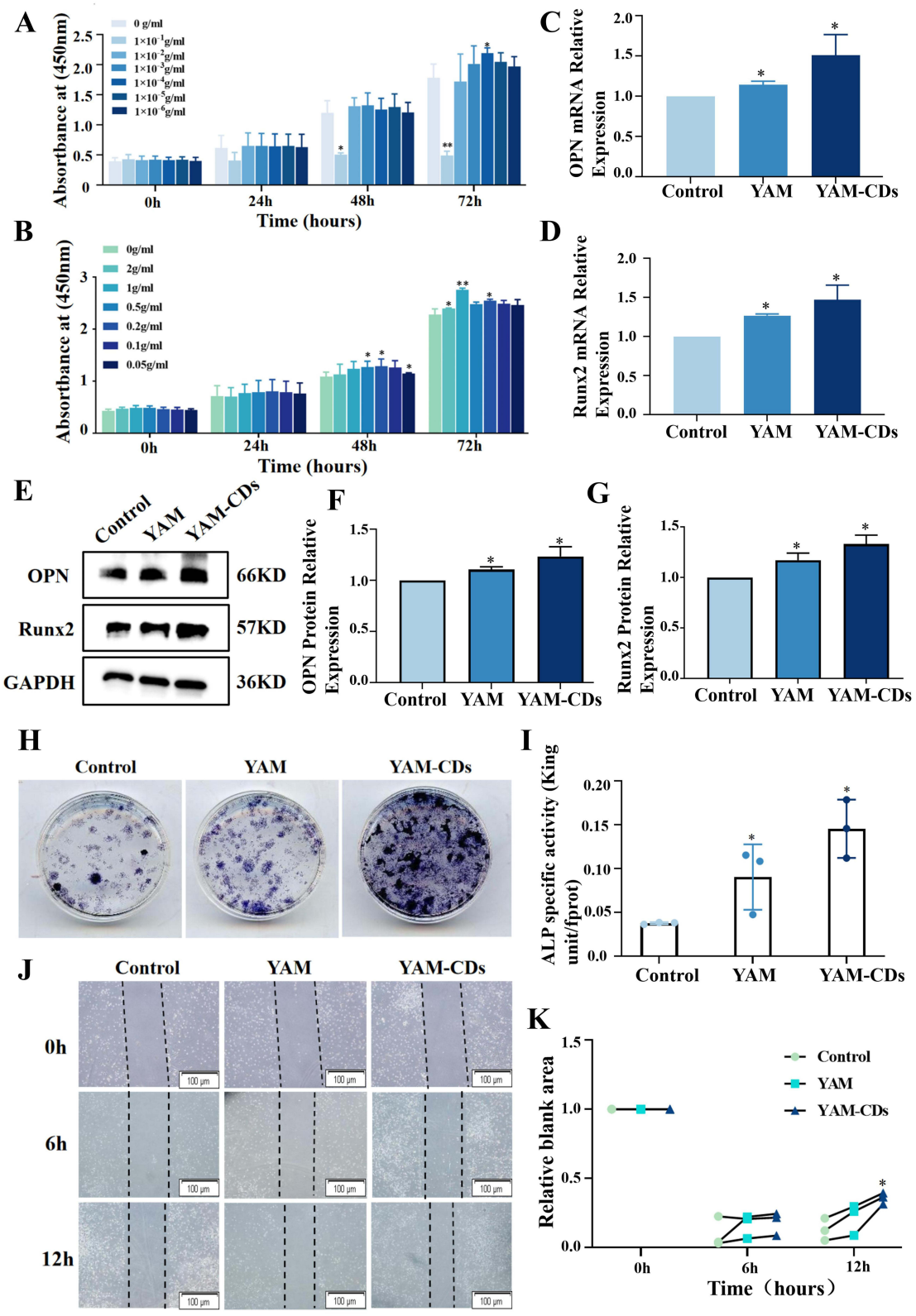

Figure 5 Functional assay of the effect of YAM-CDs in promoting osteogenic differentiation and migration. (**A** and **B**) The effect of YAM and YAM-CDs on the proliferation of BMSCs. (**C** and **D**) Graphs of the statistical results of OPN and Runx2 mRNA expression. (**E**) Graphical representation of the results of Western blotting for OPN and Runx2. (**F** and **G**) Graphs showing the statistical results of OPN and Runx2 analyzed by Western blotting. (**H**) Graph of the results of ALP staining. (**I**) Graph of statistical results of cell differentiation detected by ALP microplate assay. (**J** and **K**) Graph of cell migration results and statistical results of BMSCs (Scale bar = 100 μm) (*$p < 0.05$ **$p < 0.01$).

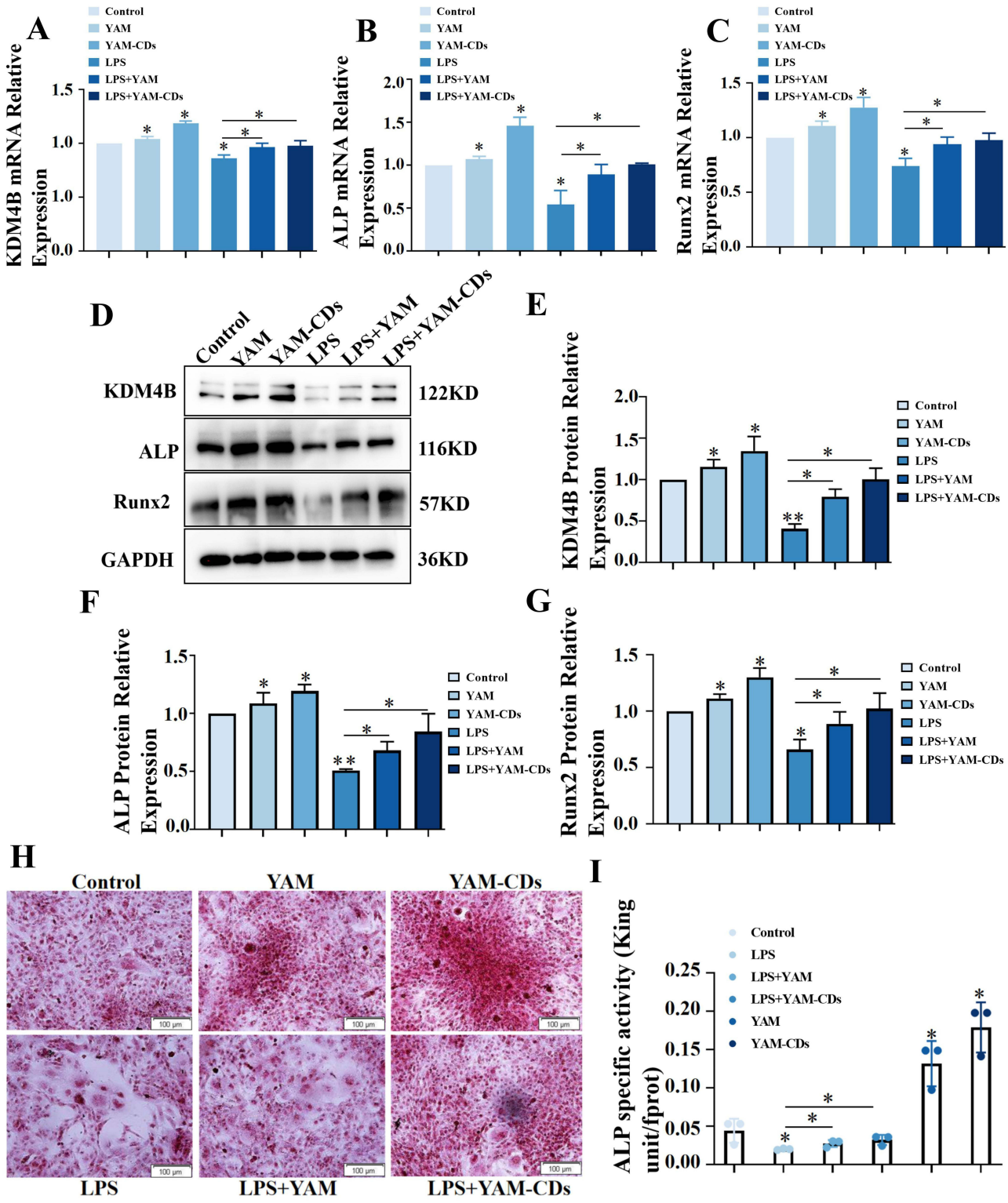

Figure 6 Effect of YAM-CDs on the gene and protein expression of osteogenesis-related factors and KDM4B. (**A**–**C**). Graph showing the statistical results of ALP, Runx2 and KDM4B mRNA expression analysis by RT-qPCR. (**D**) Graph showing the results of ALP, Runx2 and KDM4B analysis by Western blotting. (**E**–**G**). Graph of the statistical results of ALP, Runx2 and KDM4B analysis by Western blotting. (**H**) ALP staining results (Scale bar = 100 μm). (**I**) ALP microplate assay statistical results for cell differentiation (*$p < 0.05$; **$p < 0.01$).

https://doi.org/10.2147/IJN.S477587 DovePress

Effect of Knockdown of KDM4B and YAM-CDs on the Expression of Osteogenesis-Related Factors

After KDM4B-siRNA transfection in MC3T3-E1 cells for 24 h, the gene and protein expression levels in the KDM4B-siRNA group, shown in (Figure 7A–C), were significantly lower than those in the control group ($p < 0.05$), indicating that KDM4B-siRNA transfection was successful and the transfection efficiency was approximately 60%. Real-time qPCR and Western blot results (Figure 7D–H) showed that under the inflammatory microenvironment induced by LPS, expression of the osteogenesis-related factors ALP and Runx2, at both the gene and protein level, was significantly decreased after cells were transfected with KDM4B-siRNA for 24 h ($p < 0.05$). The addition of YAM-CDs or YAM resulted in a statistically-significant increase in ALP and Runx2 gene and protein expression compared to that in the KDM4B-siRNA group; the difference was statistically significant ($p < 0.05$), and the expression of ALP and Runx2 in the KDM4B-siRNA+YAM-CDs group was higher than that in the KDM4B-siRNA+YAM group ($p < 0.05$). The above

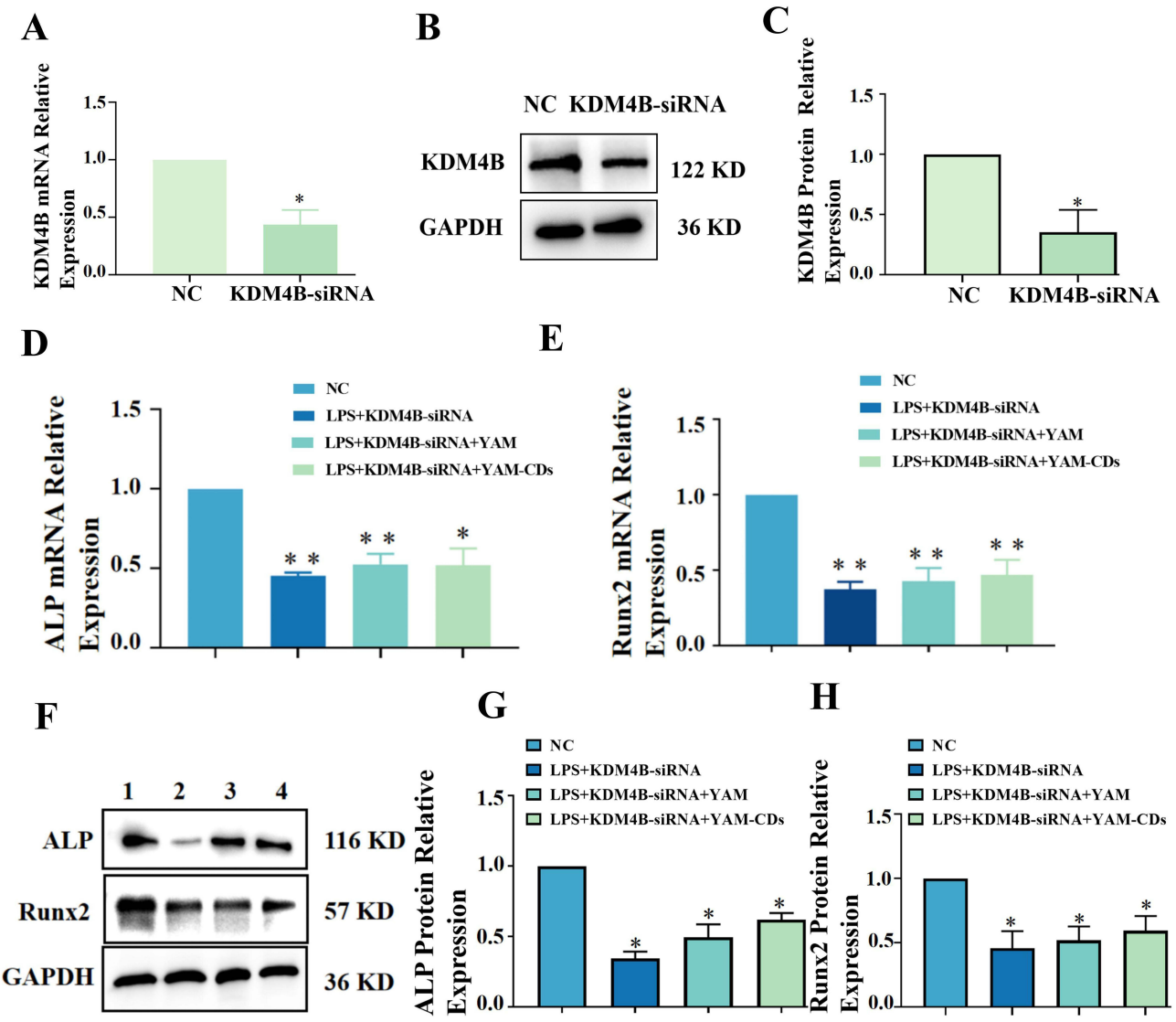

Figure 7 Knockdown of KDM4B osteogenesis-related factor expression in an LPS-induced inflammatory microenvironment. (**A**) Statistical results of KDM4B mRNA expression in MC3T3-E1 cells transfected with KDM4B-siRNA. (**B**) Protein expression of KDM4B in MC3T3-E1 cells transfected with KDM4B-siRNA. (**C**) Statistical results of KDM4B protein expression in MC3T3-E1 cells transfected with KDM4B-siRNA. (**D** and **E**) Transfection of KDM4B-siRNA, ALP and Runx2 mRNA expression in MC3T3-E1 cells. (**F**) Western blot results of ALP and Runx2 in MC3T3-E1 cells transfected with KDM4B-siRNA (1. NC; 2. LPS+KDM4B-siRNA; 3. LPS+ KDM4B-siRNA+YAM; 4. LPS+KDM4B-siRNA+YAM-CDSs). (**G** and **H**) ALP and Runx2 protein expression in MC3T3-E1 cells after transfection with KDM4B-siRNA (*$p < 0.05$; **$p < 0.01$).

results demonstrate that YAM-CDs can play a role in bone resorption or inflammatory response in periapical inflammation by inhibiting the expression of KDM4B, and then in periapical inflammation.

YAM-CDs Promote Repair of Cranial Defects in a Mouse Model

As shown in (Figure 8A), the defects in the mouse model healed well without signs of infection, scabbing, rupture, or swelling. In the control group, there was no noticeable change in the defect site, and the bone defect was not completely healed. In the gelatin methacryloyl (GEL) group, the defect was closed, and new bone tissue was visible in the defect. In the GEL+YAM-CDs group, the defect was closed entirely and filled with bone tissue. In the GEL+LPS group, the defect was still apparent, while in the GEL+LPS+YAM-CDs group, the extent of the defect was smaller than that of the GEL +LPS group, which proved that under inflammatory conditions, YAM-CDs still exhibited a bone-repairing effect.

The results of HE staining (Figure 8B) showed that the defects in the control group were only covered with a layer of periosteum, and tissue within the defects was mainly composed of fibrous connective tissue. In the GEL group, there were neoplastic trabeculae at the margins of the defects, and the bone around the defects was thickened, forming a small amount of discontinuous bone tissue. In the GEL+YAM-CDs group, continuous bone tissue was formed within the defect to close the defect, a large number of bone trabeculae were formed to thicken the bone and many osteoblasts were present on the surface of the bone trabeculae. The cranial bone of the mice in the GEL+LPS group was more damaged, there was thinning of the bone cortex, while a more significant number of osteoclasts and inflammatory cells appeared in the bone marrow cavity.

The results of Masson's trichrome staining (Figure 8C) showed that only a tiny amount of uncleanly removed bone tissue was stained light blue in the defect in the control group; a small amount of neoplastic bone tissue was stained blue in the defect in the GEL group, while normal bone tissue around the defect was red, and neoplastic bone trabeculae on the dura mater of the bone tissue were blue. In contrast, in the GEL+YAM-CDs group, a large number of newly-formed bone trabeculae at the defect were blue, the surrounding normal bone tissue was red, and the new bone trabeculae on the dura mater were blue, suggesting that the area of the defect was repaired. Mice in the GEL+LPS group had only normal bone tissue with low red collagen content and original unremoved bone at the cranial defect, almost no fresh bone tissue was formed. The results from the GEL+LPS+YAM-CDs group showed that more fresh bone tissue with a strong blue collagen fiber content was formed compared to that of the GEL+LPS group.

IHC staining was performed to investigate the expression of KDM4B, the osteogenesis-related factor OCN, and the inflammation-related factor TNF-α. Positive cells were stained dark brown. As shown in (Figure 8D and E), KDM4B and OCN were both positively expressed in more cells in the GEL+YAM-CDs group than in the GEL group, and the positive expression of KDM4B, and OCN was significantly higher in the GEL+LPS+YAM-CDs group than in the GEL+LPS group. Statistical analysis (Figure 8G and H) showed that the differences were statistically significant ($p < 0.05$; $p < 0.01$). The above results indicated that YAM-CDs enhanced the expression of the osteogenesis-related factors KDM4B and OCN in the mouse cranial defect model. As shown in Figure 8F, TNF-α was expressed in both the cytoplasm and nucleus of the cells, with the highest expression in the GEL+LPS group; the positive expression gradually decreased in the GEL+LPS+YAM-CDs, GEL, and GEL+YAM-CDs groups. In contrast the lowest number of cells with brown staining was found in the GEL+YAM-CDs group, indicating the lowest positive expression. The statistical results shown in (Figure 8I) showed significant differences ($p < 0.05$; $p < 0.01$), and indicated that YAM-CDs reduce expression of the inflammatory factor TNF-α in the mouse cranial defect model. The above results demonstrated that YAM-CDs have the ability to inhibit the inflammatory response and promote bone repair in inflammatory environments. YAM-CDs, as a novel nanoscale drug derived from traditional Chinese medicine, is expected to be a candidate for the clinical repair of inflammatory bone defects through further development of its anti-inflammatory and pro-bone-forming related mechanisms.

Discussion

The diversity of nanostructures and shapes is an important factor affecting the functionality of nanomaterials, which includes a reasonable combination of internal multicavity structures and external special shapes to consider.[29] Improving the efficiency of perfectly matching the structure and properties of nanomaterials can further enhance their functional

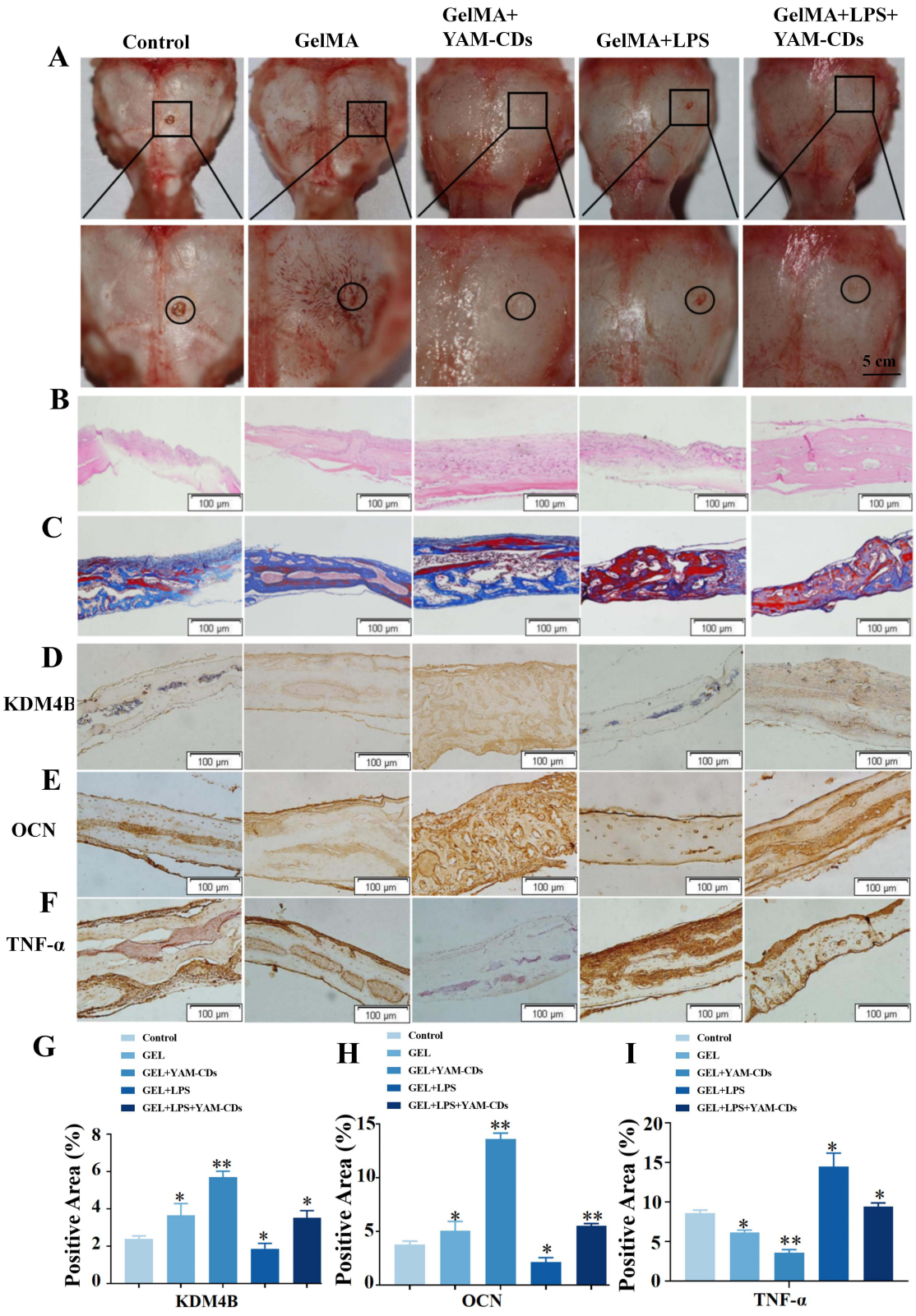

Figure 8 Diagram showing the results of studies related to the promotion of cranial defect repair in mice by YAM-CDs. (**A**) Gross observation of wound healing at the defect site in a mouse model. (**B**) HE staining of cranial defects in a mouse model. (**C**) Masson's trichrome staining of cranial defects in mice. (**D–F**). Images of immunohistochemical staining of KDM4B, OCN, and TNF-α in tissues of cranial defects in mice. (**G–I**) Statistical graphs representing the immunohistochemical staining results of KDM4B, OCN, and TNF-α positive cells (*$p < 0.05$; **$p < 0.01$).

properties or generate new functional applications.[30,31] Compared with other nanomaterials, CDs, as a new type of nanomaterials, are structurally stable and easy to be functionalized and modified, and are mainly used in bioimaging, biosensing, ion detection, and antimicrobials,[14,32–34] and thus have received widespread attention in medicine. YAM, a traditional Chinese medicine, has a variety of effects, including inhibition of the inflammatory response and promotion of bone formation.[35] TCM-CDs are CDs prepared using TCMs as the raw materials. TCM materials can be processed by physicochemical means to become CDs with a particle size of less than 10 nm,[36,37] which not only have hemostasis and anti-tumor effects, but also have the characteristics of low toxicity, good water solubility, high biocompatibility, and excellent photoluminescence performance.[38,39] There have been some studies using TCM as precursors to prepare CDs, and these synthesized TCM-CDs can not only retain their original biological activity, but also have other unique functions.[40–42] Studies have shown that CDs prepared from the Goji berry *Lycium barbarum* as raw material had better bone-enhancing effects than precursors,[43] this result is consistent with our findings. In our study, YAM was used as a precursor to synthesize YAM-CDs. According to structural characterization, YAM-CDs had a nanometer diameter and were uniformly dispersed. This allowed the YAM-CDs to enter cells and exert their pharmacological effects further. Additionally, the surface of the YAM-CDs had a large number of functional groups that ensured carbonation and dehydration during the synthetic process. C1s was the main constituent of the YAM-CDs. Their optical characterization revealed an excitation-dependent feature, a fluorescent property hardly found in other conventional drugs. In contrast to standard CDs, YAM-CDs were synthesized using medicinal components of TCM. They may contain active ingredients and chemicals derived from YAM, such as polysaccharides, phenolic compounds, and alkaloids,[44] or they may retain the medicinal value and biological activity of TCM. The yields in this investigation were higher compared to those of other studies. Further study of their biological functions will contribute to their wide application in the fields of bone defect repair, drug delivery, and targeted therapy.

Periapical bone destruction is the most common clinical feature of apical periodontitis. This condition can be brought on by any factor that interferes with osteoblast and osteoclast formation and disrupts bone homeostasis, a vital physiological function, as periapical inflammation advances.[45] In the osteogenic environment, BMSCs are regulated by bone formation-related factors and can differentiate into osteoblasts.[46] Incorporating factors promoting bone formation into the inflammatory bone resorption environment and analyzing the differentiation of BMSCs helps to provide new directions for treating clinical periapical inflammatory bone disease.[47,48] YAM-CDs were found to play a more significant role in promoting cell migration and osteogenic differentiation of BMSCs in this study when compared to YAM. Additionally, YAM-CDs were able to increase ALP staining and promote the mRNA and protein expression of factors related to osteogenesis, such as Runx2 and OPN.

Several studies have established the existence and function of cytokines in apical periodontitis. For example, thymosin-α (PTMA) inhibits inflammatory infiltration and prevents osteoclastogenesis in infected pulp, thereby preventing the development of apical periodontitis.[49] Hypoxia-inducible factor 1 (HIF-1) also plays a protective role in the development of apical periodontitis by down-regulating the expression of NF-κB and pro-inflammatory cytokines.[50] KDM4B is involved in the regulation of several physiological and pathological processes through its histone demethylase activity,[25,51,52] and, as an osteogenesis-associated factor, induces OSX by removing the demethylation of the H3K9me3 locus in the targeted homology cassette (DLX) gene family involved in OSX. Knockdown of the KDM4B gene resulted in decreased ex vivo and ex vitro osteogenic capacity of BMSCs.[53] In this study, the inflammatory microenvironment of osteoblast precursor cells was created by LPS, and the expression of KDM4B and osteogenesis-related factors was analyzed in MC3T3-E1 cells. The results revealed that YAM-CDs improved and enhanced KDM4B expression under both normal and inflammatory conditions, along with ALP and Runx2, indicating that YAM-CDs may promote bone formation through KDM4B in both situations. By down-regulating the expression of KDM4B and exploring the effect of KDM4B on bone homeostasis in a KDM4B-knockdown inflammatory microenvironment, we found that osteoblasts exhibited reduced proliferative and differentiation activities, which further clarified that YAM-CDs may promote osteoblast differentiation and maturation by regulating KDM4B. This is consistent with the findings of Yang et al,[54] who found that DLX5 promotes osteogenic/dentin differentiation by up-regulating the expression of KDM4B in apical papilla stem cells, suggesting that activation of the DLX5/KDM4B signaling pathway promoted regeneration of tissues

mediated by BMSCs of odontogenic origin. Inhibition of miR-27b-3p has been shown to enhance the expression of both KDM4B and DLX5 to relieve osteoarthritis pain.[55]

In addition to in vitro experiments, the role of YAM-CDs in bone repair was also examined in this study in a mouse model of inflammatory cranial defects,[56,57] in which a combination of YAM-CDs and GEL hydrogel[58,59] was used as a slow-release system to cover cranial defects under the action of LPS. Staining with Masson's trichrome and HE showed that a large number of new bone trabeculae were formed in the defects in the YAM-CDs group compared with the YAM group, and the new bone was tightly connected to the host bone. The results of IHC showed that KDM4B and the osteogenesis-related factor OCN were more highly expressed, while expression of TNF-α, an inflammatory factor, was lowest. These results again indicated that YAM-CDs inhibited the inflammatory response and promoted the expression of KDM4B in the inflammatory environment to promote the repair of bone defects.

This study had some limitations. Although we successfully synthesized YAM-CDs and demonstrated that YAM-CDs, as a novel nanoscale drug derived from TCM, have better therapeutic effects in inflammatory bone repair, the synthesis of CDs suffered from poor reproducibility, and CDs prepared in different batches tended to differ in fluorescence yields and sizes. Second, although YAM-CDs have shown good safety in bioimaging and sensing, it is not clear whether they will induce adverse reactions after long-term treatment. In conclusion, the application of YAM-CDs in the biomedical field is still in the preliminary stages, and there is a wide range of development opportunities and unlimited possibilities in the future.

Conclusion

In this study, we successfully prepared good biocompatible and low toxicity YAM-CDs by hydrothermal synthesis. To the best of our knowledge, the present study demonstrates for the first time that YAM-CDs stimulate osteogenic differentiation of osteoblast precursor cells, as well as migration and differentiation of BMSCs to osteoblasts, in an inflammatory environment by controlling the expression of KDM4B. And it can effectively repair the mouse cranial defect model in in vivo experiments and reduce the expression of inflammatory factors under the action of LPS. These results suggest that YAM-CDs have anti-inflammatory effects and potential to promote osteogenic differentiation. These outstanding features make YAM-CDs a safe and effective nanomedicine with good potential for application in clinical inflammatory bone disease treatment.

Acknowledgments

This work was supported by the National Natural Science Foundation of China (82100998, 82270971); Liaoning Provincial Natural Science Foundation Joint Fund (2023-MSLH-026); Provincial Basic Scientific Research Project of Liaoning Education Department (LJKZ0841); Liaoning Province Doctor Startup Fund Funded (2022-BS-237); Dalian Science and Technology Innovation Fund (2022JJ13SN063). The funders had no role in study design, data collection and analysis, decision to publish, or preparation of the manuscript.

Disclosure

QianYang Chen, Shuo liu and Yuhan Wang share first authorship. The authors report no conflicts of interest in this work.

References

1. Lyu P, Song YM, Bi RY, et al. Protective actions in apical periodontitis: the regenerative bioactivities led by mesenchymal stem cells. *Biomolecules*. 2022;12(12):1737. doi:10.3390/biom12121737
2. Liu S, Chen QY, Wang LL, et al. The novel protein complex FAPα/ITGA5 is involved in the bone destruction of apical periodontitis. *Int J Biol Macromol*. 2024;259(1):128200. doi:10.1016/j.ijbiomac.2023.128200
3. Li YZ, Yang L, Hou Y, et al. Polydopamine-mediated graphene oxide and nanohydroxyapatite-incorporated conductive scaffold with an immunomodulatory ability accelerates periodontal bone regeneration in diabetes. *Bioact Mater*. 2022;18:213–227. doi:10.1016/j.bioactmat.2022.03.021
4. Yu DG, Gong W, Zhou J, Liu Y, Zhu Y, Lu X. Engineered shapes using electrohydrodynamic atomization for an improved drug delivery. *Wiley Interdiscip Rev Nanomed Nanobiotechnol*. 2024;16(3):e1964. doi:10.1002/wnan.1964
5. Ji YX, Zhao H, Liu H, Zhao P, Yu DG. Electrosprayed stearic-acid-coated ethylcellulose microparticles for an improved sustained release of anticancer drug. *Gels*. 2023;9(9):700. doi:10.3390/gels9090700

6. Chen XH, Liu YB, Liu P. Electrospun core-sheath nanofibers with a cellulose acetate coating for the synergistic release of zinc ion and drugs. *Mol Pharm*. 2024;21(1):173–182. doi:10.1021/acs.molpharmaceut.3c00703
7. Sun L, Zhou JF, Chen YN, Yu DG, Liu P. A combined electrohydrodynamic atomization method for preparing nanofiber/microparticle hybrid medicines. *Front Bioeng Biotechnol*. 2023;11:1308004. doi:10.3389/fbioe.2023.1308004
8. Fu C, Brand HS, Bikker FJ. The applications of carbon dots in oral health: a scoping review. *Oral Dis*. 2023. doi:10.1111/odi.14702
9. Sun BH, Wu F, Zhang QC, et al. Insight into the effect of particle size distribution differences on the antibacterial activity of carbon dots. *J Colloid Interface Sci*. 2021;584:505–519. doi:10.1016/j.jcis.2020.10.015
10. Javed N, O'Carroll DM. Long-term effects of impurities on the particle size and optical emission of carbon dots. *Nanoscale Adv*. 2020;3 (1):182–189. doi:10.1039/d0na00479k
11. Ali H, Ghosh S, Jana NR. Fluorescent carbon dots as intracellular imaging probes. *Wiley Interdiscip Rev Nanomed Nanobiotechnol*. 2020;12(4): e1617. doi:10.1002/wnan.1617
12. Ran Z, Liu JK, Zhuang JL, et al. Multicolor afterglow from carbon dots: preparation and mechanism. *Small Methods*. 2024;8(1):e2301013. doi:10.1002/smtd.202301013
13. Gogoi S, Maji S, Mishra D, et al. Nano-bio engineered carbon dot-peptide functionalized water dispersible hyperbranched polyurethane for bone tissue regeneration. *Macromol Biosci*. 2017;17(3). doi:10.1002/mabi.201600271
14. Lee KK, Raja N, Yun HS, et al. Multifunctional bone substitute using carbon dot and 3D printed calcium-deficient hydroxyapatite scaffolds for osteoclast inhibition and fluorescence imaging. *Acta Biomater*. 2023;159:382–393. doi:10.1016/j.actbio.2023.01.028
15. Kanwal A, Bibi N, Hyder S, et al. Recent advances in green carbon dots (2015–2022): synthesis, metal ion sensing, and biological applications. *Beilstein J Nanotechnol*. 2022;13:1068–1107. doi:10.3762/bjnano.13.93
16. Zhang Y, Chen YM, Bai X, et al. *Glycyrrhizae radix* et rhizoma-derived carbon dots and their effect on menopause syndrome in ovariectomized mice. *Molecules*. 2023;28(4):1830. doi:10.3390/molecules28041830
17. Chen R, Ma HG, Li XP, et al. A novel drug with potential to treat hyperbilirubinemia and prevent liver damage induced by hyperbilirubinemia: carbon dots derived from *Platycodon grandiflorum*. *Molecules*. 2023;28(6):2720. doi:10.3390/molecules28062720
18. Zhao YS, Zhang Y, Kong H, et al. Carbon dots from *paeoniae radix alba* carbonisata: hepatoprotective effect. *Int J Nanomed*. 2020;15:9049–9059. doi:10.2147/IJN.S281976
19. Riekötter J, Oklestkova J, Muth J, et al. Transcriptomic analysis of Chinese yam (*Dioscorea polystachya* Turcz.) variants indicates brassinosteroid involvement in tuber development. *Front Nutr*. 2023;10:1112793. doi:10.3389/fnut.2023.1112793
20. Epping J, Laibach N. An underutilized orphan tuber crop-Chinese yam: a review. *Planta*. 2020;252(4):58. doi:10.1007/s00425-020-03458-3
21. Zhang N, Liang TS, Jin Q, et al. Chinese yam (Dioscorea opposita Thunb.) alleviates antibiotic-associated diarrhea, modifies intestinal microbiota, and increases the level of short-chain fatty acids in mice. *Food Res Int*. 2019;122:191–198. doi:10.1016/j.foodres.2019.04.016
22. Hwang JH, Park YS, Kim HS, et al. Yam-derived exosome-like nanovesicles stimulate osteoblast formation and prevent osteoporosis in mice. *J Control Release*. 2023;355:184–198. doi:10.1016/j.jconrel.2023.01.071
23. Kim S, Shin MY, Son KH, et al. Yam (Dioscorea batatas) root and bark extracts stimulate osteoblast mineralization by increasing Ca and P accumulation and alkaline phosphatase activity. *Prev Nutr Food Sci*. 2014;19(3):194–203. doi:10.3746/pnf.2014.19.3.194
24. Ni FJ, Tang HT, Cheng ST, et al. KDM4B: a promising oncology therapeutic target. *Cancer Sci*. 2024;115(1):8–16. doi:10.1111/cas.16005
25. Wang ZZ, Cai HR, Zhao EH, Cui HJ. The diverse roles of histone demethylase KDM4B in normal and cancer development and progression. *Front Cell Dev Biol*. 2022;9:790129. doi:10.3389/fcell.2021.790129
26. Zhang X, Nan H, Guo JL, Liu JY. KDM4B overexpression promotes the growth, migration, and invasion of rheumatoid arthritis fibroblast-like synoviocytes by activating STAT3 pathway. *Biochem Genet*. 2021;59(6):1427–1440. doi:10.1007/s10528-021-10042-1
27. Lee HL, Yu B, Deng P, Wang CY, Hong C. Transforming growth factor-β-induced KDM4B promotes chondrogenic differentiation of human mesenchymal stem cells. *Stem Cells*. 2016;34(3):711–719. doi:10.1002/stem.2231
28. Deng P, Yuan Q, Cheng YD, et al. Loss of KDM4B exacerbates bone-fat imbalance and mesenchymal stromal cell exhaustion in skeletal aging. *Cell Stem Cell*. 2021;28(6):1057–1073.e7. doi:10.1016/j.stem.2021.01.010
29. Liu YB, Chen XH, Lin XD, et al. Electrospun multi-chamber core-shell nanofibers and their controlled release behaviors: a review. *Wiley Interdiscip Rev Nanomed Nanobiotechnol*. 2024;16(2):e1954. doi:10.1002/wnan.1954
30. Champion JA, Katare YK, Mitragotri S. Particle shape: a new design parameter for micro- and nanoscale drug delivery carriers. *J Control Release*. 2007;121(1–2):3–9. doi:10.1016/j.jconrel.2007.03.022
31. Yang YW, Nie D, Liu Y, Yu MR, Gan Y. Advances in particle shape engineering for improved drug delivery. *Drug Discov Today*. 2019;24 (2):575–583. doi:10.1016/j.drudis.2018.10.006
32. Giordano MG, Seganti G, Bartoli M, Tagliaferro A. An overview on carbon quantum dots optical and chemical features. *Molecules*. 2023;28 (6):2772. doi:10.3390/molecules28062772
33. Shen YZ, Nie C, Pan T, et al. A multifunctional cascade nanoreactor based on Fe-driven carbon nanozymes for synergistic photothermal/ chemodynamic antibacterial therapy. *Acta Biomater*. 2023;168:580–592. doi:10.1016/j.actbio.2023.07.006
34. Dehvari K, Chiu SH, Lin JS, Girma WM, Ling YC, Chang JY. Heteroatom doped carbon dots with nanoenzyme like properties as theranostic platforms for free radical scavenging, imaging, and chemotherapy. *Acta Biomater*. 2020;114:343–357. doi:10.1016/j.actbio.2020.07.022
35. Obidiegwu JE, Lyons JB, Chilaka CA. The *Dioscorea* Genus (Yam)—an appraisal of nutritional and therapeutic potentials. *Foods*. 2020;9(9):1304. doi:10.3390/foods9091304
36. Li D, Xu KY, Zhao WP, et al. Chinese medicinal herb-derived carbon dots for common diseases: efficacies and potential mechanisms. *Front Pharmacol*. 2022;13:815479. doi:10.3389/fphar.2022.815479
37. Wang XK, Wu T, Yang YX, et al. Ultrasmall and highly biocompatible carbon dots derived from natural plant with amelioration against acute kidney injury. *J Nanobiotechnology*. 2023;21(1):63. doi:10.1186/s12951-023-01795-5
38. Zeng MT, Wang Y, Liu MZ, et al. Potential efficacy of herbal medicine-derived carbon dots in the treatment of diseases: from mechanism to clinic. *Int J Nanomed*. 2023;18:6503–6525. doi:10.2147/IJN.S431061
39. Zhao YS, Kong H, Li YR, et al. Inhibitory effects of *Curcumae Radix carbonisata*-based carbon dots against liver fibrosis induced by carbon tetrachloride in mice. *Artif Cells Nanomed Biotechnol*. 2024;52(1):23–34. doi:10.1080/21691401.2023.2239522

40. Zhu XF, Zhou Y, Yan SH, et al. Herbal medicine-inspired carbon quantum dots with antibiosis and hemostasis effects for promoting wound healing. *ACS Appl Mater Interfaces*. 2024;16(7):8527–8537. doi:10.1021/acsami.3c18418
41. Wen FZ, Li PY, Yan HJ, Su W. Turmeric carbon quantum dots enhanced chitosan nanocomposite films based on photodynamic inactivation technology for antibacterial food packaging. *Carbohydr Polym*. 2023;311:120784. doi:10.1016/j.carbpol.2023.120784
42. Zhang ML, Cheng JJ, Luo J, et al. Protective effects of *Scutellariae Radix Carbonisata*-derived carbon dots on blood-heat and hemorrhage rats. *Front Pharmacol*. 2023;14:1118550. doi:10.3389/fphar.2023.1118550
43. Guo ZY, Wang ZL, Liu YG, et al. Carbon dots from *Lycium barbarum* attenuate radiation-induced bone injury by inhibiting senescence via METTL3/Clip3 in an mA-dependent manner. *ACS Appl Mater Interfaces*. 2023;15(17):20726–20741. doi:10.1021/acsami.3c01322
44. Zhu PD, Wang SY, Zhang YQ, et al. Carbon dots in biomedicine: a review. *ACS Appl Bio Mater*. 2022;5(5):2031–2045. doi:10.1021/acsabm.1c01215
45. Bordukalo-Nikšić T, Kufner V, Vukičević S. The role of BMPs in the regulation of osteoclasts resorption and bone remodeling: from experimental models to clinical applications. *Front Immunol*. 2022;13:869422. doi:10.3389/fimmu.2022.869422
46. Liu ZT, Wang YX, Liu FY, et al. Long noncoding TSI attenuates aortic valve calcification by suppressing TGF-β1-induced osteoblastic differentiation of valve interstitial cells. *Metabolism*. 2023;138:155337. doi:10.1016/j.metabol.2022.155337
47. Yang MM, Shen ZS, Zhang XF, et al. Ferroptosis of macrophages facilitates bone loss in apical periodontitis via NRF2/FSP1/ROS pathway. *Free Radic Biol Med*. 2023;208:334–347. doi:10.1016/j.freeradbiomed.2023.08.020
48. Luo JX, Chen HY, Wang GF, et al. CGRP-loaded porous microspheres protect BMSCs for alveolar bone regeneration in the periodontitis microenvironment. *Adv Healthc Mater*. 2023;12(28):e2301366. doi:10.1002/adhm.202301366
49. Gong QM, Lv XM, Liao CX, et al. Single-cell RNA sequencing combined with proteomics of infected macrophages reveals prothymosin-α as a target for treatment of apical periodontitis. *J Adv Res*. 2024;17:S2090–1232(24)00031–6. doi:10.1016/j.jare.2024.01.018
50. Hirai K, Furusho H, Hirota K, Sasaki H. Activation of hypoxia-inducible factor 1 attenuates periapical inflammation and bone loss. *Int J Oral Sci*. 2018;10(2):12. doi:10.1038/s41368-018-0015-0
51. Wang ZZ, Cai HR, Li ZK, Sun W, Zhao EH, Cui HJ. Histone demethylase KDM4B accelerates the progression of glioblastoma via the epigenetic regulation of MYC stability. *Clin Epigenetics*. 2023;15(1):192. doi:10.1186/s13148-023-01608-4
52. Sha JJ, Han Q, Chi CF, et al. Upregulated KDM4B promotes prostate cancer cell proliferation by activating autophagy. *J Cell Physiol*. 2020;235(3):2129–2138. doi:10.1002/jcp.29117
53. Ye L, Fan ZP, Yu B, et al. Histone demethylases KDM4B and KDM6B promotes osteogenic differentiation of human MSCs. *Cell Stem Cell*. 2012;11(1):50–61. doi:10.1016/j.stem.2012.04.009
54. Yang HQ, Fan J, Cao YY, Gao RT, Fan ZP. Distal-less homeobox 5 promotes the osteo-/dentinogenic differentiation potential of stem cells from apical papilla by activating histone demethylase KDM4B through a positive feedback mechanism. *Exp Cell Res*. 2019;374(1):221–230. doi:10.1016/j.yexcr.2018.11.027
55. Zhang GX, Zhou Y, Su MM, Yang XC, Zeng BY. Inhibition of microRNA-27b-3p relieves osteoarthritis pain via regulation of KDM4B-dependent DLX5. *Biofactors*. 2020;46(5):788–802. doi:10.1002/biof.1670
56. Szpalski C, Barr J, Wetterau M, Saadeh PB, Warren SM. Cranial bone defects: current and future strategies. *Neurosurg Focus*. 2010;29(6):E8. doi:10.3171/2010.9.FOCUS10201
57. Asada Y, Koshinuma S, Mikami M, et al. Comparison of the wound-healing efficacy of gelatin sponge dressings and that of artificial dermis using atelocollagen in a rat cranial periosteal defect model. *Exp Anim*. 2022;71(2):161–172. doi:10.1538/expanim.21-0049
58. Wang HN, Zou Q, Boerman OC, et al. Combined delivery of BMP-2 and bFGF from nanostructured colloidal gelatin gels and its effect on bone regeneration in vivo. *J Control Release*. 2013;166(2):172–181. doi:10.1016/j.jconrel.2012.12.015
59. Mamidi N, Ijadi F, Norahan MH. Leveraging the recent advancements in GelMA scaffolds for bone tissue engineering: an assessment of challenges and opportunities. *Biomacromolecules*. 2024;25(4):2075–2113. doi:10.1021/acs.biomac.3c00279